Original Research

ONCOLOGY

Targeted photothermal therapy of hepatocellular carcinoma using gold nanoparticles functionalized with anti-cadherin and folic acid in a validated murine model

Meda Cosma[1], Teodora Mocan[1,2], Teodora Pop[2,3], Ofelia Mosteanu[2,3], Romelia Pop[4], Flaviu Tabaran[4], Lucian Mocan[2,3]

1) Department of Physiology, "Iuliu Hatieganu" University of Medicine and Pharmacy, Cluj Napoca, Romania

2) Nanomedicine Department, Regional Institute of Gastroenterology and Hepatology, Cluj Napoca, Romania

3) 3rd Surgery Clinic, "Iuliu Hatieganu" University of Medicine and Pharmacy, Cluj Napoca, Romania

4) University of Agricultural and Veterinary Medicine, Cluj Napoca, Romania

Abstract

Background. Hepatocellular carcinoma (HCC) remains a major therapeutic challenge with limited treatment options. Nanotechnology, particularly the use of gold nanoparticles (GNPs), offers new perspectives for targeted photothermal therapies.

Objective. This study aimed to develop and evaluate the effectiveness of nanomediated photothermal therapy (PTT) using GNP functionalized with folate and anti-Cadherin-1 antibodies (Cad-1) in the treatment of HCC in a validated murine model.

Methods. A bionanosystem composed of gold nanoparticles conjugated with polyethyleneimine (PEI), folic acid (FA), and Cad-1 was synthesized and characterized. A HCC murine model was induced by administration of diethylnitrosamine and carbon tetrachloride. After tumor confirmation, animals were divided into four groups and treated with different doses of the nanoconstruct, followed by near-infrared (NIR) laser irradiation (808 nm). A total of 16 animals were allocated into four experimental groups (n = 4 per group). Histological analysis and serum biochemical assays (aspartate aminotransferase (AST), alanine aminotransferase (ALT), alkaline phosphatase (ALP) and gamma-glutamyl transferase (GGT)) were performed.

Results. The treatment induced focal coagulative necrosis within tumor regions, with minimal impact on surrounding healthy liver tissue. Significant reductions in AST and GGT levels were observed in animals treated with higher doses ($p < 0.05$), confirming the efficacy and selectivity of the therapy. Immunohistochemistry confirmed E-cadherin overexpression in tumor tissue, suggesting a possible diagnosic potential for the targeting system.

Conclusion. The GNPs-PEI-FA-Cad-1 system demonstrated promising results for targeted photothermal therapy in HCC, with selective tumor ablation and limited hepatotoxicity. The validated murine model provides a robust platform for preclinical assessment of similar nanotherapies.

Keywords: hepatocellular carcinoma, gold nanoparticles, photothermal therapy, targeted nanotherapy, murine models

DOI: 10.15386/mpr-2905

Manuscript received: 14.04.2025
Received in revised form: 07.07.2025
Accepted: 08.07.2025

Address for correspondence:
Meda Cosma
manolea.meda@umfcluj

Introduction and objectives

According to GLOBOCAN data, liver cancer is the sixth most commonly diagnosed cancer worldwide, with 866,136 new cases reported, and it ranks as the third leading cause of cancer-related mortality, accounting for 758,725 deaths globally. Notably, there is a marked gender disparity, with men being affected at nearly twice the rate observed in women [1].

Currently, treatment modalities for hepatocellular carcinoma include liver transplantation, local ablation, surgical resection, transarterial chemoembolization, and transarterial radioembolization with yttrium-90 (Y90) [2]. However, the rate of curative interventions is unfortunately only around 20% [3], leaving chemotherapy as the final treatment option. However chemotherapy has several limitations. The effectiveness of systemic treatments, such as sorafenib, is modest, with a median survival of less than a year and a low tumor response rate. Additionally, options are limited for patients with extrahepatic metastases or vascular invasion. Hepatic arterial infusion chemotherapy shows promising results, but there is no clear evidence that it is superior to systemic chemotherapy. Furthermore, side effects such as hand-foot syndrome and fatigue affect patients' quality of life [4]. This highlights the urgent need for the development of new multimodal therapeutic approaches.

Nanotechnology applications in cancer therapy have opened promising avenues for improving treatment outcomes and extending patient survival.

One such approach is based on the unique physicochemical properties of gold nanoparticles. Dimensionally, these nanoparticles range between 1–100 nm, and their shape varies from spherical to more complex forms such as tetrahedral, nanorods, or nanocubes. The size and shape directly influence their behavior within the body, affecting distribution, tumor retention time, systemic toxicity, and renal clearance rate, with studies showing that particles around 6 nm can be efficiently eliminated through renal filtration.

The surface chemistry of gold nanoparticles is another important attribute, as they have high bioinertness and low toxicity compared to other metallic nanoparticles, making them suitable for in vivo applications. Their surface can be easily functionalized, allowing the attachment of ligands, antibodies, polymers, or chemotherapeutic drugs, providing stability and enabling them to specifically target tumor cells. An important example of a functionalizing agent is polyethyleneimine, a positively charged polymer that improves the stability of nanoparticles in the bloodstream and facilitates their uptake by tumor cells through electrostatic interactions with cell membranes [5].

Previous studies have shown that highly proliferative HCC cells present loss of E-cadherin from the cell membrane, followed by epithelial-mesenchymal transition and increased cell migratory properties [6]. The loss represents the results of proteolytic (ADAM/MMP) cleavage of the membrane protein [7]. The resulting fragment routes are giving rise to soluble E-cadherin (se-Cadherin), an 80 kDa protein fragment that is released in the extracellular fluid, blood and represents a negative biomarker, being associated with invasiveness, angiogenesis and poor prognosis [8]. However, E-cadherin may also be detached from the membrane and processed as VE-cadherin through endocytosis/and lysosomal or proteasomal processing [9].

The latter mechanism, a particular intracellular processing pathway, opens novel possibilities for intracellular targeting via antibody-mediated delivery systems.

Folate receptors type FRα are known to be overexpressed in ovarian, breast, and lung cancer. They have recently been demonstrated as upregulated in certain types of hepatocellular carcinoma and therefore have become favorite for nanocarrier experimental membrane targeting approaches in HCC. Moreover, the folate -based membrane targeting approach in HCC additionally benefits from a secondary uptake mechanisms. The liver benefits from reduced folate carrier, essential for folate uptake in hepatocytes [10]. All evidences support the use of folate as a membrane targeting element in HCC.

An essential aspect of gold nanoparticles relates to their remarkable optical properties, due to the phenomenon of localized surface plasmon resonance (LSPR), which consists of the collective oscillation of conduction electrons when the particles are exposed to light at specific wavelengths. This property gives them a tunable absorption spectrum, from visible to near-infrared (700–1000 nm), allowing their use in deep-tissue medical imaging and in therapies such as photothermal therapy, where exposure to NIR laser light induces heat generation in targeted tissues. This heat leads to protein denaturation, mitochondrial damage, and disruption of the cell membrane, processes that ultimately result in cell death through apoptosis or necrosis [11]. In HCC, PTT is particularly indicated for localized tumors, being useful both for patients who are not eligible for surgical interventions and as an adjuvant treatment to reduce the risk of post-resection recurrence. It can also be combined with systemic therapies or immunotherapy, improving treatment efficacy by stimulating both local and systemic immune responses [12].

Thus, targeted gold nanoparticle therapy combined with PTT represents a minimally invasive, precise alternative with reduced adverse effects in the management of HCC, contributing to the expansion of therapeutic options for patients with this condition.

The aim of this study was to develop and characterize a targeted bio-nanostructured system based on GNPs functionalized with folate (for membrane targeting) anti-Cadherin-1 antibodies (for intracellular targeting), designed for the selective delivery of nanoparticles and subsequent

NIR laser-mediated photothermal ablation of HCC cells, while minimizing damage to normal hepatic tissue.

Methods

To develop the proposed therapeutic system, gold nanoparticles were synthesized and functionalized, followed by in vivo testing in a validated murine model of chemically induced HCC. Subsequently, a targeted photothermal therapy was applied. $HAuCl_4 \bullet 3H_2O$ (≥ 99% trace metal basis), crystalline L-ascorbic acid, polyvinylpyrrolidone (PVP) K60, and sodium hydroxide (NaOH) pellets were purchased from Sigma-Aldrich. Ethanol (≥ 99.90%) was obtained from Sigma, and double-distilled water (ddH_2O) was produced in-house. All solutions were prepared using purified water (resistivity ≈ 18.2 MΩ•cm). Glassware was thoroughly rinsed with distilled water, ethanol, and acetone, and dried in an oven prior to use. Freshly prepared solutions were used unless otherwise noted; stock solutions were used only when indicated. Anti-Cadherin-1 antibody solutions were prepared in RNase-free water following Sigma-Aldrich guidelines.

Colloidal gold nanoparticles were synthesized using a modified Turkevich method, in which L-ascorbic acid served as the reducing agent and PVP was used as the stabilizer [13]. The reducing solution was prepared by dissolving L-ascorbic acid in absolute ethanol or in binary solvent mixtures of ethanol and water at volumetric ratios of 20%, 50%, or 80%. PVP was added directly into the L-ascorbic acid/ethanol-water solvent mixture to a final concentration of 1% (w/v), under low-intensity sonication. The pH of the reducing solution was adjusted to 10.5 by dropwise addition of 2 M NaOH.

The total water volume added to the ethanol-water binary mixture was calculated using the equation:

$$\%\ \mathbf{water\ volume} = \frac{(Vw + VGC)}{VR} \times 100$$

Where *Vw* is the volume of water, *VGC* is the volume of the $HAuCl_4$ solution, and *VR* is the total reaction volume.

The GNP-forming reaction mixture was prepared by rapid injection of an aqueous $HAuCl_4$ solution (5 mM) into the reducing solution. The total reaction volume was maintained at 20 mL ($HAuCl_4$ and L-ascorbic acid). The initial concentrations were: $HAuCl_4$ – 0.15 mM and ascorbic acid – 1.5 mM (molar ratio 1:10). The reaction mixture was stirred at 800 rpm for 30 minutes at room temperature, and the resulting colloid was filtered (Whatman filter) and stored at 4°C to prevent further reaction.

The optimization of the GNPs focused on specific properties that enhance anti-Cadherin delivery while reducing potential cytotoxicity. These properties include surface complexity and the size of the GNPs. Thus, we developed a GNP-based targeted therapy system to deliver anti-Cadherin antibodies into liver cancer tumor cells. The negatively charged Cad-1 antibodies were subsequently coated with folic acid on the GNP-PEI via electrostatic interactions, forming stable anionic complexes.

Surface modification was performed in sequential steps. First, the GNPs were coated with a layer of polyethylenimine, rendering the particles cationic. For GNP-PEI synthesis, 1.42 mL of PEI (2.3 mM) was added to 32.6 mL of 1 mM $HAuCl_4$ solution, followed by 0.5 mL of freshly prepared 100 mM ascorbic acid.

The solution was left to react overnight at room temperature.

In the next step, activated folic acid was prepared: 0.25 g (5.663×10^{-4} mol) of folic acid was homogenized in 10 mL of dry DMSO, followed by the addition of 0.125 mL (8.960×10^{-4} mol, 1.5 equivalents) of triethylamine to facilitate the solubilization and activation of the carboxyl groups. The resulting solution was sonicated for 10 minutes and then further mixed until the folic acid was completely dissolved. Subsequently, 0.13 g (1.1295×10^{-3} mol, ~2 equivalents) of N-hydroxysuccinimide (NHS) and 0.235 g (1.138×10^{-3} mol, ~2 equivalents) of N,N′-dicyclohexylcarbodiimide (DCC) were added to activate the folic acid. In the final step, the negatively charged Cad-1 antibodies (IGG-CF) were coated with the activated folic acid and added to the GNP-PEI through electrostatic interaction, generating stable anionic GNP-PEI-FA-Cad-1 complexes.The functionalized nanoparticles (GNPs-PEI-FA-Cad-1) were characterized using multiple complementary analytical techniques.

The UV-visible (UV-Vis) extinction spectra of each GNP sample were recorded at ambient temperature (25 °C) using a Shimadzu UV-Vis spectrophotometer. The maximum surface plasmon resonance (SPR) wavelength of the resulting GNPs was determined from the UV-Vis data to estimate particle size.

The UV-Vis spectrum of the gold colloid solution (10 mL) was recorded over the wavelength range of 350–800 nm using a Jasco V-530 UV-VIS spectrophotometer. In order to more accurately estimate the diameter of the synthesized gold nanospheres, UV-Vis spectrum simulations were performed depending on particle radius. These simulations were based on Mie theory and conducted using an online absorption spectrum simulation tool (www.nanoHUB.org), which considers nanoparticle size and composition.

UV-Visible characterization of GNP solutions at various concentrations was performed using a UV-Vis-NIR spectrophotometer with an optical resolution of 0.4 nm. Absorbance measurements were carried out over a wavelength range of 200–800 nm using 1 cm path length quartz cuvettes. Prior to each use, the cuvettes were cleaned by sonicating them for 5 minutes in deionized water and

rinsing with deionized water. The pH of all analyzed solutions remained stable at 6.4.

Particle size distribution, zeta potential, mean particle size, size distribution profile, polydispersity index (PDI), and zeta potential of the GNPs were measured using a Malvern Zetasizer Nano ZS instrument. The PDI was calculated from the intensity-based particle size distribution (PSD) graphs obtained from dynamic light scattering (DLS) measurements.

DLS analysis of all GNP suspensions was conducted using a Zetasizer Nano ZS90 DLS system (Malvern Instruments Ltd., UK), equipped with a green laser (532 nm, 4 mW) and a photodiode detector with a quantum efficiency >50% at 532 nm. The measured scattering light intensity was reported as a photon count rate (kcps – kilocounts per second). Due to differences in scattering intensity caused by particle size variation, the power of the incident laser beam was adjusted using the instrument's built-in attenuator to maintain an optimal photon count rate. The attenuation level was indexed according to specific attenuation settings. Malvern DTS 5.10 software was used for data processing and analysis. All reported average particle sizes are based on intensity-weighted means. For each sample suspension, two DLS measurements were performed, with a fixed run time of 20 s. The scattering angle was set at 90°.

Atomic force microscopy (AFM) measurements were performed using a TT-AFM® instrument (AFMWorkshop, CA, USA) operated in non-contact mode and equipped with ACTA-SS cantilevers (AppNano, CA, USA). The biofunctionalized nanoparticles were deposited onto mica substrates using a KLM® SCC spin coater (Schaefer Technologie GMBH, Langen, Germany). Data interpretation was carried out using Gwyddion® 2.36 software.

All AFM images were corrected solely for tip artifacts and surface tilt, then analyzed using the mentioned software. Particle size analysis was conducted via the particle and pore analysis module in the SPIP software. An automatic threshold was applied to each image, excluding particles smaller than 7 nm from the analysis. Histograms and kernel density plots were generated to evaluate nanoparticle height distribution. All reported density curves were constructed using 512 points and a Gaussian kernel function. Peak heights were extracted by fitting the density curve to a Gaussian minimum using PeakFit software, with both peak height and Gaussian width being recorded.

Additionally, to confirm the presence of antibodies and their interaction with the nanoparticle surface, attenuated total reflectance Fourier-transform infrared spectroscopy (ATR-FTIR) was applied. This technique provided information about the secondary structure of proteins and the functional groups involved in the surface functionalization process.

The HCC experimental model was developed in *Mus musculus* mice maintained under standard vivarium conditions (65% humidity, 21 °C temperature, 12-hour light/dark cycle, standardized food, and ad libitum access to water), as can be seen in figure 1, in accordance with European Directive 63/2010 and Romanian Law no. 43/2014. Animals were provided by the Center for Experimental Medicine and Practical Skills – Biobase, Iuliu Haţieganu University of Medicine and Pharmacy, Cluj-Napoca. The experiment was conducted at the Biobase of the "Prof. Dr. O. Fodor" Regional Institute of Gastroenterology and Hepatology, a certified facility (authorization no. 894/07.12.2020), re-evaluated in 2022 as a low-risk research unit. The experimental protocol was approved by the Sanitary-Veterinary Authority (approval no. 268/12.07.2021).

Figure 1. Aspects of animals in the housing environment.

The toxic hepatocarcinoma model (n=8) was induced by administering a single intraperitoneal dose of diethylnitrosamine (DEN, 100 mg/kg), followed by chronic administration of carbon tetrachloride (CCl_4, 0.5 mL/kg) twice weekly for 8 weeks. Animals were continuously monitored throughout the experimental protocol. Tumor nodule development was monitored by sacrificing the animals, and all animals were euthanized according to ethical guidelines via an overdose of ketamine/xylazine anesthesia to ensure no pain or distress.

For validation of the experimental model, the first step after euthanasia was to secure the animal onto the dissection board as shown in figure 2.

Figure 2. Preparation for post-euthanasia dissection steps, with the animal fixed onto the dissection board.

Palpation to detect any hepatic irregularities was followed by dissection of the skin and muscle layers, with evaluation of macroscopic pathological features, and subsequently by histopathological analysis of the hepatic tumor masses.

After validating the reproducible experimental HCC model, the next step was the application of in vivo NIR photothermal therapy mediated by gold nanoparticles.

In total, sixteen mice were used, with four animals per group. The number of animals per group followed the minimal recommendations in the literature (n=4/group) to ensure statistical relevance regarding biodistribution and treatment efficacy [14]. Following confirmation of tumor development, animals were randomly divided into four experimental groups based on the intravenous dose of nanoconstruct administered:

- **Group 1 (n=4):** HCC group, receiving intravenous injection of a maximal concentration solution of the nanocomposite (approximately 50 µg/mL). After 24 hours, administration was followed by laser irradiation applied to the skin over the tumor site (808 nm, 3 min, 5 sessions).
- **Group 2 (n=4):** HCC group, receiving intravenous injection of a medium concentration solution of the nanocomposite (approximately 25 µg/mL). After 24 hours, administration was followed by laser irradiation applied to the skin over the tumor site (808 nm, 3 min, 5 sessions).
- **Group 3 (n=4):** HCC group, receiving intravenous injection of a low concentration solution of the nanocomposite (approximately 12.5 µg/mL). After 24 hours, administration was followed by laser irradiation applied to the skin over the tumor site (808 nm, 3 min, 5 sessions).
- **Group 4 (n=4):** HCC group, without nanocomposite administration and without subsequent irradiation.

All equipment was calibrated to ensure uniform irradiation and precise therapeutic delivery.

The results were compared with those of the HCC validation control group, consisting of healthy mice that did not undergo carcinogenesis induction.

Before euthanasia, blood samples were collected via retro-orbital puncture for hepatic function analysis, including AST, ALT, GGT, and ALP. Macroscopic findings, including animal deaths or other observations at endpoint, were recorded and documented photographically.

All invasive procedures were performed under intraperitoneal anesthesia to ensure animal welfare. In cases of severe health deterioration, early humane euthanasia was performed using anesthetic overdose. At the end of the experiment, the animals were euthanized by administering an overdose of anesthetic.

After planned euthanasia (overdose of ketamine/xylazine, with no recovery from anesthesia), tissue samples were collected from the liver, fixed in 10% neutral-buffered formalin, and processed according to standard histological protocols [15]. Histopathological examination allowed assessment of tumor burden, identification of post-treatment necrotic areas, and evaluation of structural changes. Immunohistochemistry was also performed to determine E-cadherin expression, confirming the specificity of the targeted therapeutic approach.

This study was approved by the National Sanitary Veterinary and Food Safety Authority (ANSVSA) (approval no. 268/12.07.2021). All animal procedures complied with institutional and national ethical guidelines.

Results

Gold nanoparticles were designed and optimized as delivery vehicles for anti-Cad-1 in vivo**.** Optimization efforts focused on nanoparticle surface complexity and size—key parameters for improving delivery efficiency and reducing potential cytotoxicity. As a result, we developed a biofunctional nanocomplex, intended for molecularly targeted therapy in hepatocellular carcinoma.

Gold nanoparticles display a unique optical feature known as localized surface plasmon resonance, representing the collective oscillation of conduction electrons in resonance with a specific wavelength of incident light. The LSPR effect produces a strong absorbance band in the visible range (500–600 nm), measurable via UV-Vis spectroscopy. The LSPR peak is highly dependent on nanoparticle size and shape. As the particle diameter increases, the peak wavelength shifts toward the red region of the spectrum; additionally, non-spherical particles further alter the absorption pattern compared to spherical ones of the same size.

The UV-Vis spectrum of the gold colloid solution (10 mL) was recorded over the wavelength range of 350–

800 nm using a Jasco V-530 UV-Vis spectrophotometer. The spectrum presents a distinct absorption band with a maximum at 522 nm and a full width at half maximum (FWHM) of approximately 50 nm. This absorption band is characteristic of spherical gold nanoparticles and is attributed to the surface plasmon resonance generated by the interaction between the conduction electrons and the incident electromagnetic radiation. Notably, the UV-Vis profile shown in figure 3, Panel A was reproducible several weeks post-synthesis, confirming the colloidal stability of the synthesized nanoparticles.

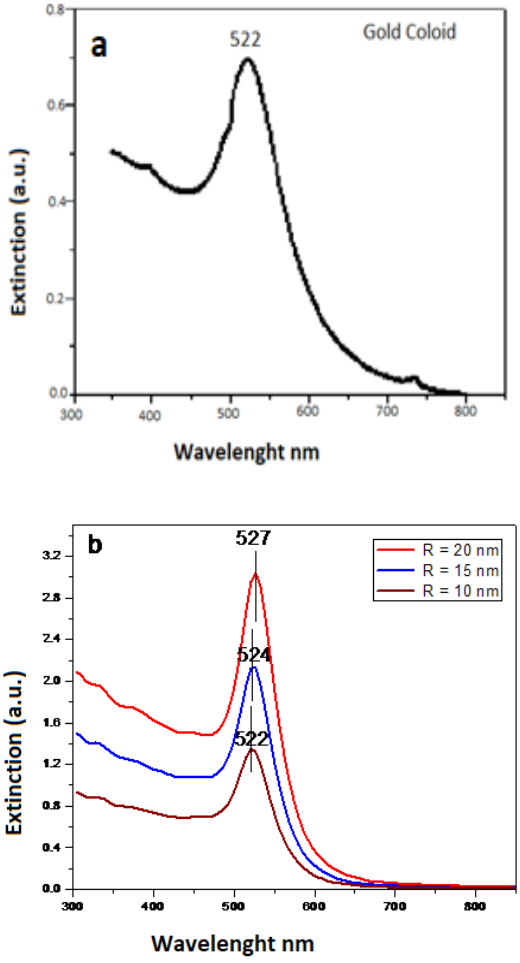

Figure 3. (a) UV-Vis spectrum of the gold colloid solution. **(b)** Simulated UV-Vis spectra of the gold colloid as a function of the radius of the spherical gold nanoparticle.

As shown in figure 4**,** the GNPs were analyzed by UV-Vis spectroscopy, which revealed a red shift in the surface plasmon resonance (SPR) peaks upon the addition of anti-Cad-1 antibodies.

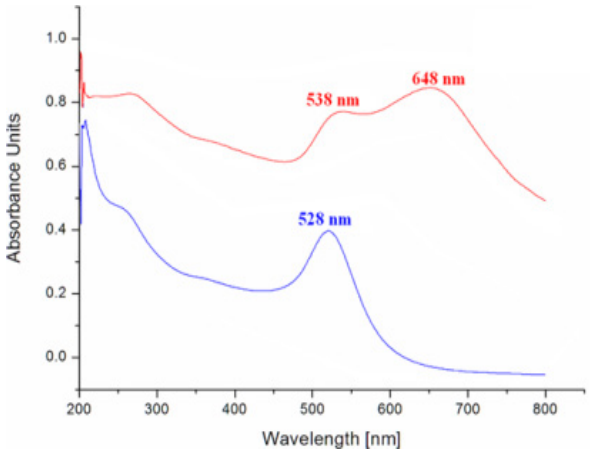

Figure 4. UV-Vis analysis of the GNP-PEI-FA-Cad-1 solution (red spectrum).

DLS measurements revealed the hydrodynamic diameters of the different nanoparticle complexes (Figure 5): GNPs (12.82 nm), GNP-PEI (18.97 nm), GNP-PEI-Cad-1 (39.59 nm), and GNP-PEI-FA-Cad-1 (47.25 nm), indicating a progressive increase in particle size with each additional functionalization step.

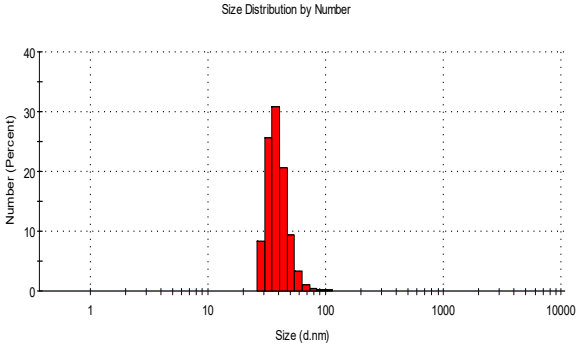

Figure 5. Hydrodynamic diameter of the GNP-PEI-FA-Cad-1 bionanocomplex**.**

The GNPs were initially coated with an inner layer of thiol-modified polyethyleneimine (HS-PEI), forming gold–sulfur bonds that rendered the particles cationic. Negatively charged Cad-1 antibodies were then conjugated, along with folic acid, onto the GNP-PEI surface via electrostatic interactions, resulting in anionic complexes. By adjusting the concentration of the outer PEI layer in the GNP-PEI-Cad-1 complexes, the overall surface charge shifted from negative to positive.

Zeta potential measurements confirmed the surface charge of each nanostructure**:** GNPs (−33.8 mV), GNP-PEI (+44.7 mV), GNP-PEI-FA-Cad-1 (−36.7 mV), and GNP-PEI-FA-Cad-1 after adjusting PEI concentration

(+52.4 mV). These results demonstrated successful synthesis and optimization of the GNP-Cad-1 nanocomplexes.

It is well known that rotational diffusion of highly scattering, non-spherical particles with diameters greater than 30–40 nm may result in false intensity peaks in the 5–10 nm range. In such cases, non-critical application of DLS can lead to discrepancies in volume or number-based size distributions compared to those obtained via AFM. Additionally, for particles with weak dynamic diffusion and diameters below 20 nm, DLS often shows an additional broad peak in the higher size range, attributed to nanoparticle aggregates or secondary product particles rather than to individual nanoparticles.

Importantly, DLS can be used to detect conjugate aggregation of gold nanoparticles triggered by biospecific interactions at their surface.

Figure 6 shows the AFM image of the synthesized GNP-PEI-FA-Cad-1 bionanostructures**.** The nanostructures exhibited a spherical morphology with an average measured diameter of approximately 40.4 nm. The differences between DLS and AFM measurements can be attributed to the nature of the techniques: DLS provides information on the hydrodynamic diameter, which includes solvation layers surrounding the nanoparticle, whereas AFM measures the physical particle size in the dry state.

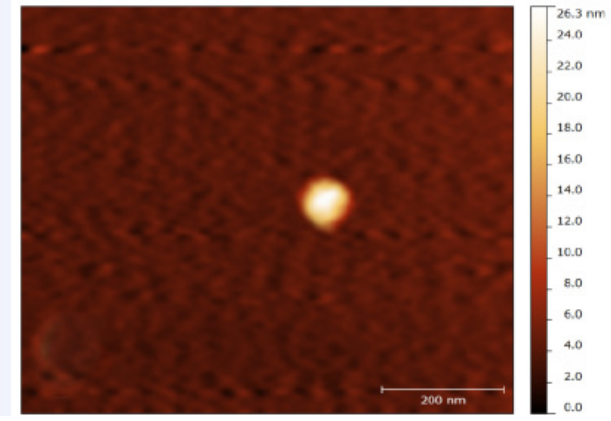

Figure 6. AFM image of the synthesized GNP-PEI-FA-Cad-1 bionanostructure.

The GNP-PEI-FA-Cad-1 bionanostructure was subjected to infrared (IR) spectroscopy analysis, a technique that provides insights into the secondary structure of proteins.

The IR absorption band at 1637 cm^{-1} corresponds to amide I, which is attributed to C=O stretching vibrations, while the band at 1534 cm^{-1} corresponds to amide II, associated with C–N stretching and N–H bending vibrations within the β-sheet structures of IgG molecules.

The presence of these two characteristic protein bands, along with the disappearance of citrate-associated peaks at 1590 and 1370 cm^{-1}, confirms the successful functionalization of the gold nanoparticles with IgG-CF.

Regarding the validation of the experimental model, after dissection of the skin and muscle layers, macroscopic changes in the liver could be observed through the transparency of the peritoneum. The observed changes were inconclusive, ranging from transperitoneally visible nodular hepatic structures to large masses that caused conformational changes in the upper abdominal region, as seen in Figure 7, panel A.

Deeper dissection confirmed these findings in the animals used for validation of the HCC model. Figure 7 panel B, shows macroscopically visible, moderately well-defined, heterogeneous nodular liver tumors within the hepatic parenchyma, observed in one of the sacrificed mice from the validation group.

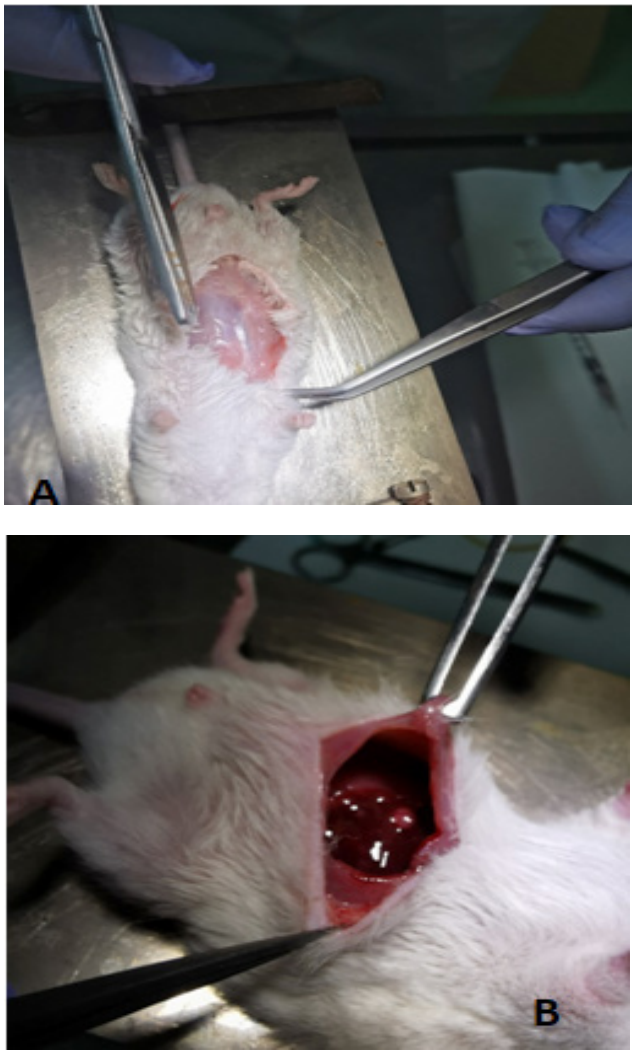

Figure 7. (A) Dissection of the skin and muscle layers with evaluation of visible pathological features through the transparent peritoneum. **(B)** Dissection of the peritoneal cavity and macroscopic evaluation of the structure, size, and conformation of the peritoneal organs.

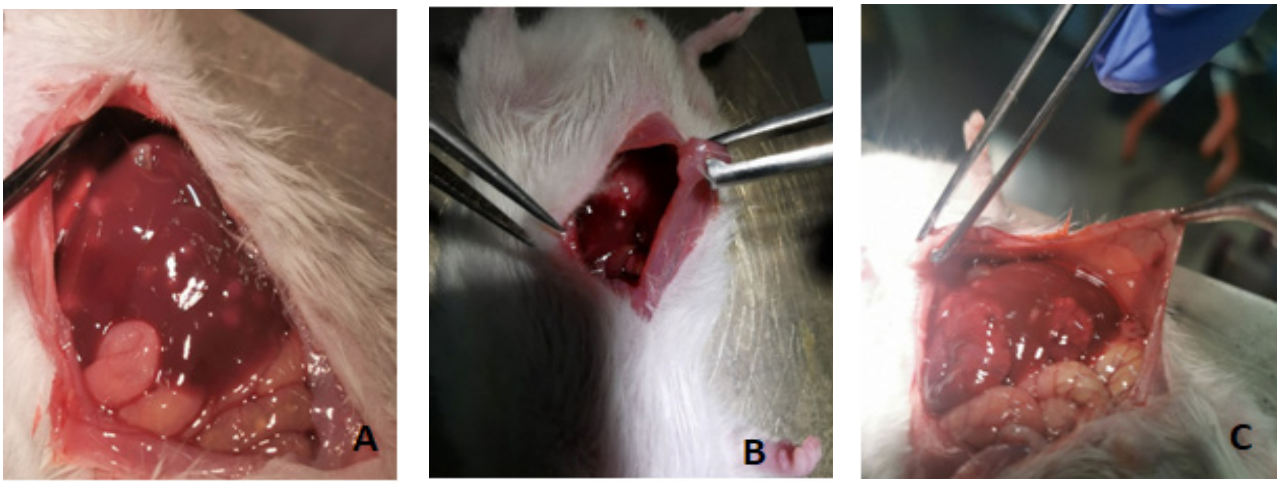

Figure 8. Macroscopic variations in the appearance of tumors induced during the carcinogenesis protocol.
(A) Small, multiple, nodular formations; **(B)** Large, poorly demarcated nodular tumors, reduced in number; **(C)** Tumors with pronounced neoplastic characteristics (large size, irregular shape, poor delimitation from surrounding normal tissue, heterogeneous structure with included vascular formations, microhemorrhages, calcifications), as well as satellite parenchymal dissemination.

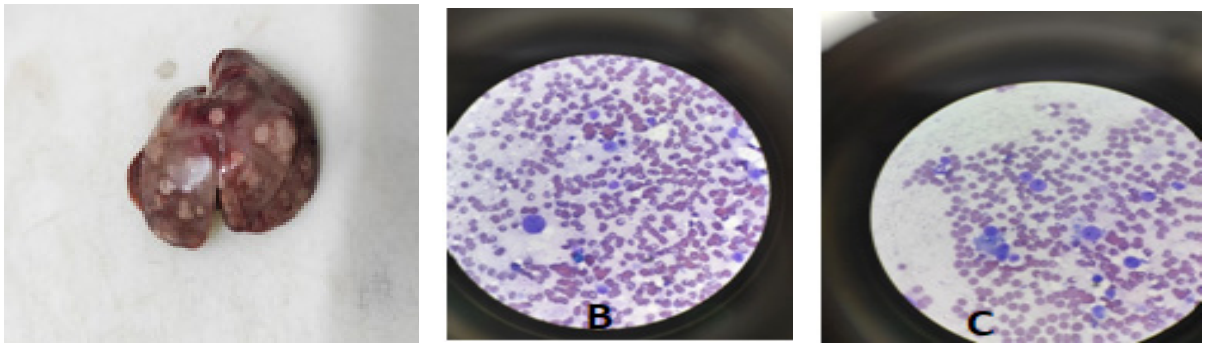

Figure 9. Morphopathological analysis of the detected tumor structures. **(A)** Macroscopic features; **(B, C)** Cytological features of hepatic tissue following the HCC induction protocol.

Tumor masses induced by the carcinogenic treatment were observed in the majority of the mice by the end of the validation period. The macroscopic appearance of these lesions varied considerably, ranging from small, multiple, heterogeneous nodular formations (Figure 8, panel A), to larger, solitary or sparsely distributed nodules that were poorly demarcated from the surrounding healthy liver tissue (Figure 8, panel B). In some cases, the tumors appeared as large, heterogeneous masses—either solitary or multiple—exhibiting pronounced malignant characteristics in terms of shape, size, structure, localization, and evidence of secondary dissemination (Figure 8, panel C).

Dissection and isolation of the organs and tissues were followed by cytological analysis of the samples collected from the liver tumors. Figure 9 illustrates the macroscopic appearance of the liver after fixation (panel A), as well as the observed microscopic characteristics—cells with malignant features, including large size, multiple nuclei, and atypical morphologies (panel B). These features became more pronounced with the progression of the carcinogenesis induction protocol. Panel C shows extensive malignant changes interspersed with normal hepatocytes, characteristic of hepatocellular carcinoma.

Histopathological images of chemically induced (untreated) tumors reveal the transition between normal hepatic parenchyma (black asterisk) and chemically induced tumor tissue (white asterisk) as shown in figure 10, panel A.

Panel B presents the detailed architecture of the chemically induced tumor, characterized by compact nodules of hepatocytes exhibiting moderate pleomorphism, arranged in hepatic cords exceeding 4–5 cells in thickness**.** This histological pattern is consistent with the diagnosis of differentiated hepatocellular carcinoma**,** as defined by current classification criteria [16].

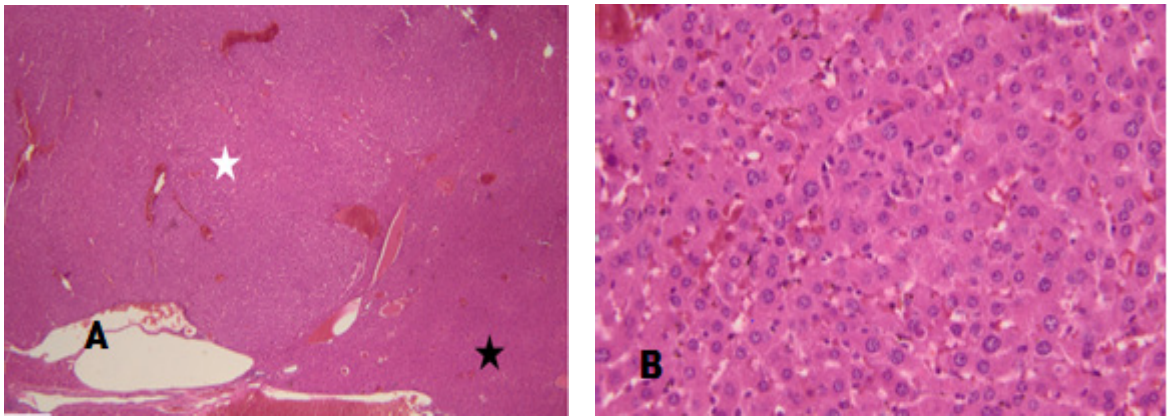

Figure 10. Histopathological features of chemically induced tumors. **(A)** HE, objective x10, **(B)** HE, objective x40.

In comparison with the experimental group, the histological structure of the control group, used to validate the experimental model, displayed a normal and homogeneous hepatic architecture, with no signs of morphological alteration. There was no evidence of hepatocyte clustering or architectural disorganization, and the trabecular arrangement of the hepatic parenchyma remained well preserved.

Moreover, no cytological changes suggestive of cellular stress, inflammation, or nuclear pleomorphism were observed. The overall histological appearance indicated a physiologically stable state, with no signs of tumor involvement or response to external agents, as can be seen in figure 11, thus confirming the validity and relevance of using this group as a reference for interpreting the results in treated animals.

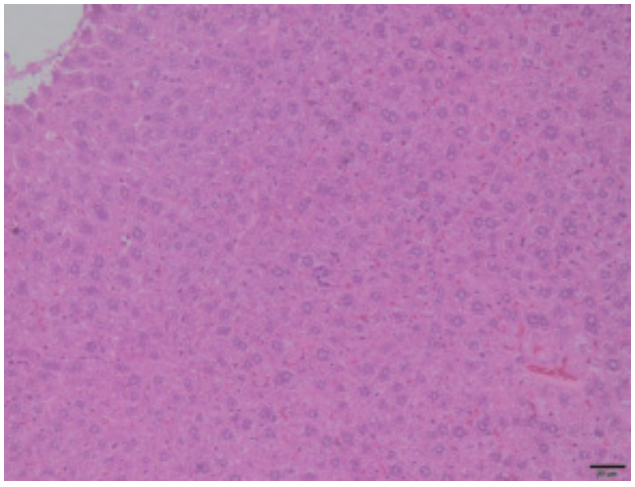

Figure 11. Histological appearance of hepatic tissue from the control group used for HCC model validation (untreated group, without pro-carcinogenic substances or therapeutic interventions).

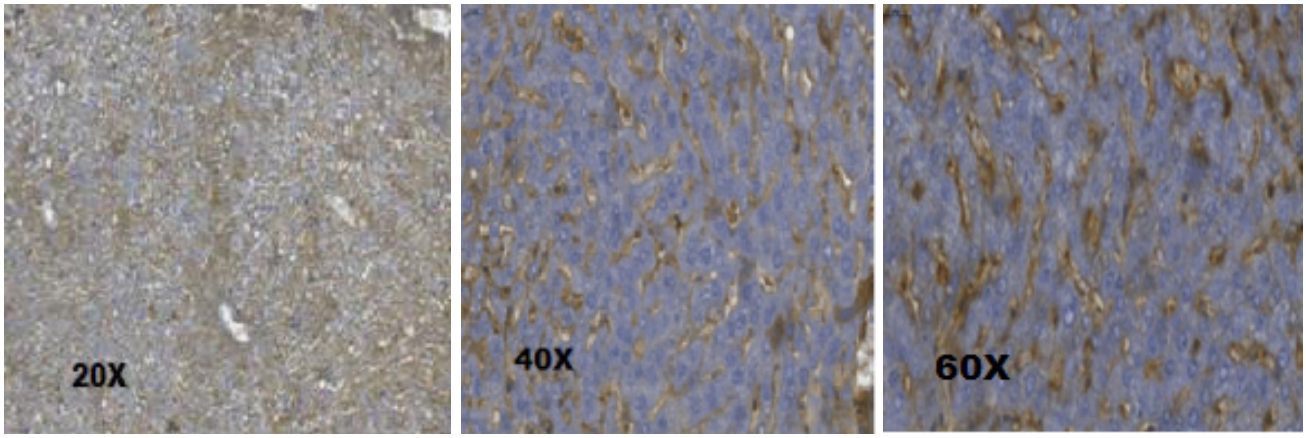

Figure 12. E-cadherin expression in tumor regions, highlighting its role as a targeting and selective marker for photothermal therapy (immunohistochemical staining).

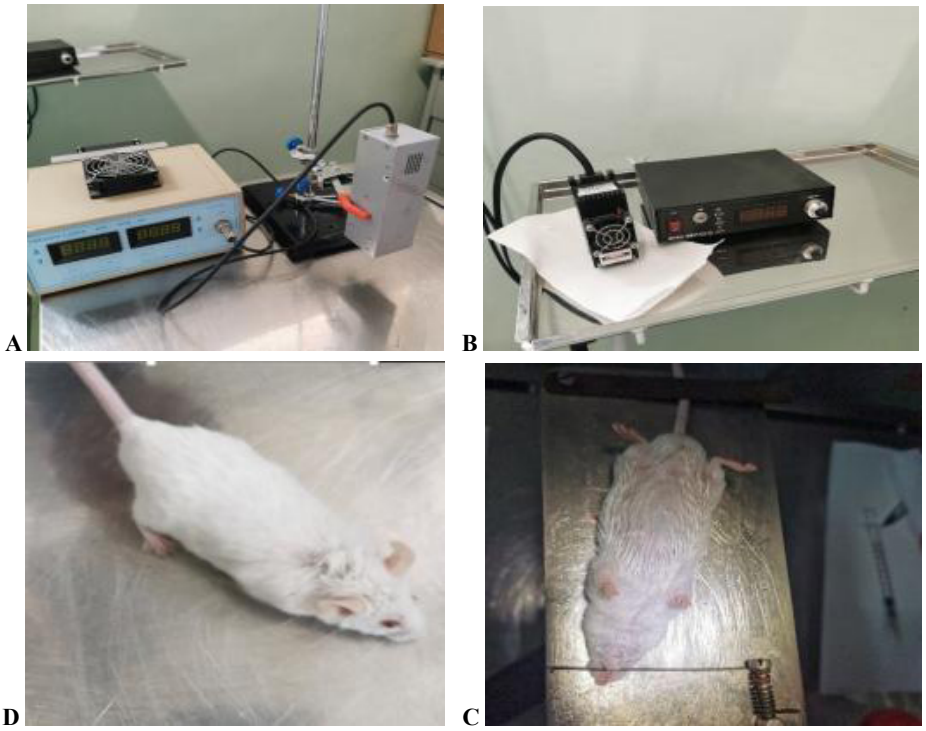

Figure 13. Steps involved in the photothermal treatment procedure. **(A, B)** Equipment used for laser irradiation; **(C, D)** Preparation of the experimental animal through anesthesia and fixation onto the dissection platform.

Increased expression of E-cadherin in tumor regions was confirmed by immunohistochemical analysis**,** highlighting its potential as a targeting marker for photothermal therapies. As shown in figure 12, E-cadherin is predominantly expressed at the cell membrane level of tumor cells, enabling selective recognition by anti-Cad-1 antibodies functionalized on gold nanoparticles.

This specific distribution supports the use of E-cadherin as a molecular target for the precise delivery of treatment and the controlled accumulation of the nano-therapeutic system within the tumor microenvironment.

The main experimental steps are illustrated in figure 13 involved in the implementation and validation of the photothermal treatment. The process began with the preparation (panels A and B) and calibration of the laser irradiation system, including verification of equipment functionality and emission parameters.

Simultaneously, general anesthesia was induced to ensure complete immobilization of the animal during laser exposure, following a standard protocol involving intraperitoneal administration of a xylazine-ketamine mixture.

The animal was then positioned and securely fixed on the dissection board (panel D), ensuring proper exposure of the target region. The optical module responsible for delivering the laser radiation was mounted and precisely adjusted to ensure uniform energy distribution across the treatment area and minimize inter-individual variability in irradiation.

This step was critical for standardizing the photothermal treatment and achieving reproducible experimental outcomes.

Detectable histological effects were observed in the group that received the highest concentration of the nanoconstruct. The treatment outcomes for group 1 are shown in figure 14.

Panels A and B reveal focal areas of coagulative necrosis (indicated by asterisk), accompanied by minimal perilesional reaction. In addition, individual hepatocyte necrosis can be seen in localized regions (indicated by arrows), without prominent surrounding histological response.

These findings support the notion of selective targeting achieved by the nanomediated photothermal treatment**,** as the coagulative necrosis was confined to specific tumor areas while preserving surrounding healthy hepatic tissue**.**

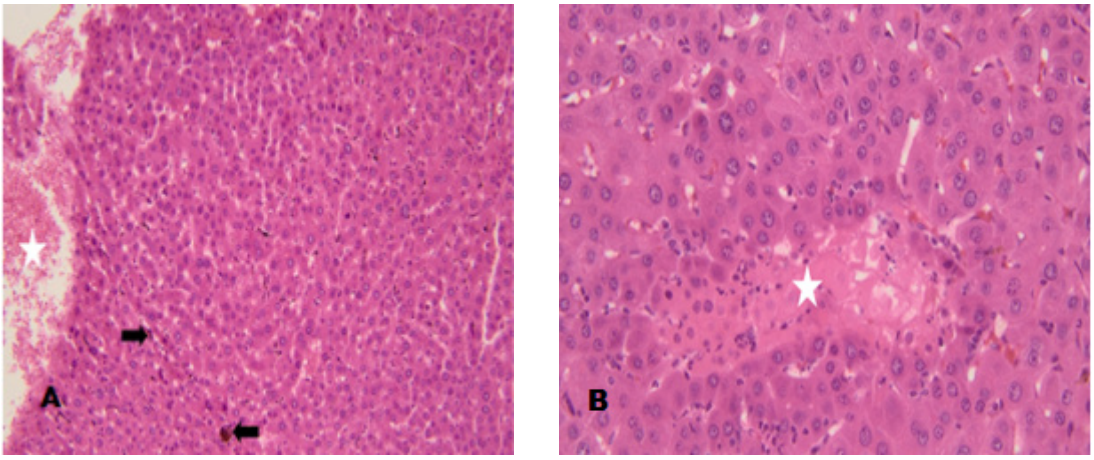

Figure 14. Histological features after administration of the nanoconstruct followed by laser irradiation (808 nm, 3 min). **(A)** HE, objective x10, **(B)** HE, objective x40.

The functional impact of the treatment was assessed by measuring key liver function biomarkers: AST, ALT, ALP, and GGT.

AST levels showed statistically significant differences between groups ($p < 0.05$). The adjacent figure (Figure 15) presents the mean AST values recorded for each group. The most pronounced reduction in AST was observed in the group treated with the highest concentration of nanoconstruct (50 µg/mL), with a mean value of 133.7 ± 11.4 U/L, compared to 165.7 ± 4.04 U/L in the untreated HCC group.

The hepatoprotective effect—reflected by the reduction in hepatocytolytic activity—was less evident in groups treated with 25 µg/mL (143.0 ± 11.1 U/L) and 12.5 µg/mL (160.3 ± 9.45 U/L). Notably, AST values in the lowest-dose group approached those observed in the untreated HCC group, suggesting a dose-dependent therapeutic response.

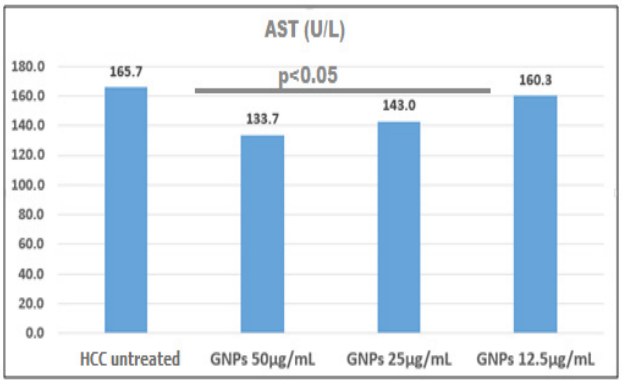

Figure 15. Plasma AST values for the untreated HCC group and the groups treated with serial concentrations of the GNP-based nanoconstruct, followed by laser irradiation. Error bars represent standard deviation.

Serum ALT levels ranged from 128.0 ± 2.0 U/L in the untreated HCC group to slight decreases in the group receiving 12.5 µg/mL of nanoconstruct (122.7 ± 7.6 U/L), moderate reductions in the 25 µg/mL group (119.3 ± 7.02 U/L), and a more marked decrease in the group treated with the maximum dose (119.7 ± 17.5 U/L).

Although these differences were not statistically significant ($p > 0.05$), the trend closely mirrored the pattern observed for AST levels, as illustrated in figure 16.

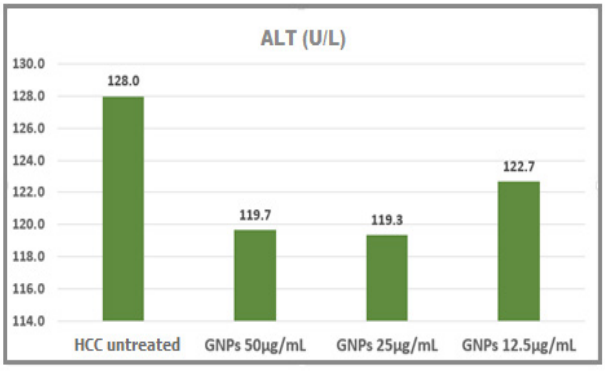

Figure 16. Plasma ALT values for the untreated HCC group and the groups treated with serial concentrations of the GNP-based nanoconstruct, followed by laser irradiation. Error bars represent standard deviation.

As can be seen in figure 17, ALP concentrations across the experimental groups were comparable, with no statistically significant differences observed between them ($p > 0.05$). The measured values were as follows: 80.4 ± 0.92 U/mL in the untreated HCC group, 79.5 ± 0.9 U/mL in the group treated with the highest concentration of gold nanoparticle-based nanoconstruct, 74.7 ± 4.5 U/mL in the 25 µg/mL group, and 74.13 ± 5.23 U/mL in the 12.5 µg/mL group.

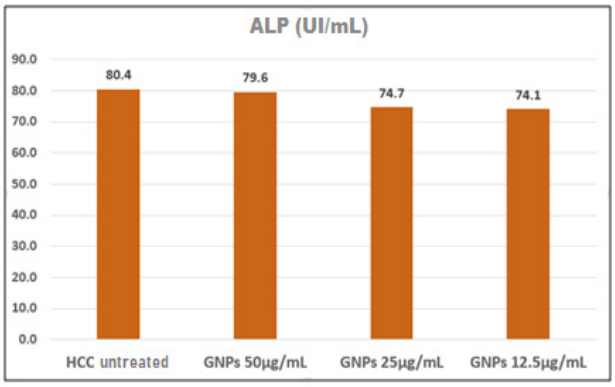

Figure 17. Plasma ALP values for the untreated HCC group and the groups treated with serial concentrations of the GNP-based nanoconstruct, followed by laser irradiation. Error bars represent standard deviation.

Serum GGT levels showed substantial reductions in the treatment groups receiving 50 µg/mL (53.1 ± 5.6 U/mL) and 25 µg/mL (54.9 ± 13.3 U/mL) concentrations of GNP-based nanoconstructs, when compared to both the untreated HCC group (87.8 ± 3.4 U/mL) and the group treated with gold nanoparticles alone, without targeted functionalization (87.8 ± 2.21 U/mL).

The observed differences were statistically significant ($p < 0.05$), as shown in figure 18.

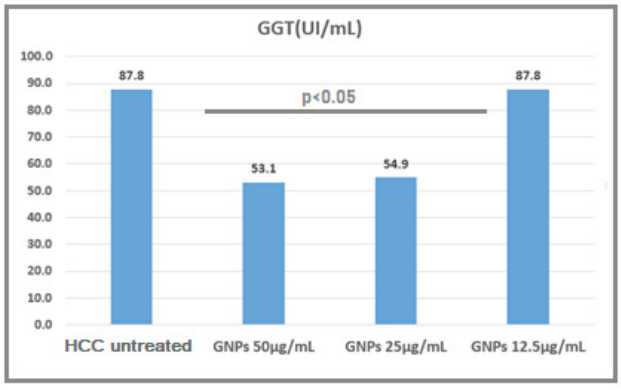

Figure 18. Plasma GGT values for the untreated HCC group and the groups treated with serial concentrations of the GNP-based nanoconstruct, followed by laser irradiation. Error bars represent standard deviation.

Discussion

The results obtained in this study support the feasibility of using a bionanostructured system based on functionalized gold nanoparticles for targeted photothermal therapy of hepatocellular carcinoma in a validated murine model, offering promising perspectives for expanding minimally invasive therapeutic options for this pathology.

Data obtained through UV-Vis spectroscopy, DLS, and AFM confirmed the morphological and optical characteristics of the functionalized nanoparticles, their long-term colloidal stability, and their size, which is suitable for accumulation within the tumor microenvironment. Changes in zeta potential after each functionalization step confirmed the successful anchoring of PEI, folic acid, and Cad-1 antibodies on the nanoparticle surface, optimizing their properties for targeted delivery.

Chemically induced models of HCC are known to trigger tumor formation via two mechanisms: direct induction of DNA damage and, more recently described, the facilitation of tumor promotion through hepatotoxic agents that promote clonal expansion of preneoplastic cells [17,18].

The DEN-based HCC model is well recognized for its reproducibility and for inducing oxidative stress through accumulation of reactive oxygen species (ROS) such as superoxide anions and hydrogen peroxide. DEN is also known to alkylate cellular DNA.

Most studies describe a typical progression of DEN-induced hepatic lesions—from basophilic foci and hyperplastic nodules to hepatocellular adenomas and ultimately hepatocellular carcinoma [19]. The features described in the literature largely overlap with the changes we observed during tumor development. In our study, the model exhibited slow development, with tumors requiring at least 12 months to form.

The literature notes the influence of factors such as sex, age, and strain on tumor progression rates [17,20]. Our animals were two weeks old at protocol initiation—a threshold between neonatal and juvenile stages. Although early age is typically associated with accelerated HCC progression due to active hepatocyte proliferation [17,19], tumor development in our model was slow, likely due to the lack of additional promoters in mice older than two weeks.

To address this limitation, we included CCl_4 in the experimental protocol. While commonly used as a pro-fibrotic agent in hepatic fibrosis models, CCl_4 also induces epidermal growth factor (EGF) expression, promoting hepatic regeneration and facilitating tumor progression.

The confirmation of increased cadherin presence in tumor regions through immunohistochemistry validates the molecular targeting strategy employed, in line with literature data highlighting the overexpression of this cell adhesion molecule in rapidly proliferating HCC cells.

An important aspect highlighted by our data is the remarkable selectivity of NIR laser-induced photothermal treatment on tumos masses, with minimal impact on healthy hepatic parenchyma. This effect is attributed to both the optical properties of gold nanoparticles, characterized by the LSPR phenomenon, and the specific targeting achieved through the combined folate-based membrane targeting and anti-Cadherin-1 antibodies-based intracellular delivery.

From a functional standpoint, while conventional chemotherapies generally exclude patients with elevated

AST/ALT due to drug-induced cytolysis and enzyme release, our results showed an opposite effect. Treatment led to reduced AST and ALT levels, especially at higher nanoconstruct concentrations. This could be explained by the mode of cell destruction: while drug-induced lysis causes membrane rupture and enzyme release, thermal ablation inactivates cellular components—including hepatocellular enzymes—in the treated zone.

Possible explanations could be due to coagulative necrosis process, in which hydrolytic enzymes, such as proteases, are denatured before they can digest cells. Moreover, low pH and hypoxia denature both structural proteins and lysosomal enzymes. All those mechanisms may induce slow clearance of dead tissue [21].

In the case of ALP, no significant differences were observed under treatment. A possible explanation is the initially low tumor expression of this marker in murine liver tissue, as euthanasia occurred at early HCC stages. Extended timelines allowing further tumor progression may yield more significant changes.

Conversely, GGT levels decreased significantly in treated groups, especially at higher nanoconstruct concentrations. Our findings align with other studies using different nanophotothermal platforms. Zhou et al. reported promising results using GGT as a targeting element in fluorescence-guided photothermal therapy [22]. Similarly, Li et al. proposed fluorescently labeled GGT for in vitro tumor cell identification, enabling targeted photothermal ablation using near-infrared light [23].

Furthermore, the presence of folic acid moiety of the nanoconstruct could be one possible explanation for the protective effects recorded. Several other publications have demonstrated reduced oxidative injury, increased antioxidant protection (glutathione peroxidase, catalase, superoxide dismutase) [24,25].

Future studies should focus on evaluating the long-term therapeutic efficacy of GNP-based photothermal therapy and monitoring potential tumor recurrence in hepatocellular carcinoma models. It will also be essential to assess the biodistribution, clearance pathways, and potential off-target effects of the functionalized nanoparticles to ensure safety and translational applicability. Combining GNP-mediated photothermal therapy with other treatment modalities, such as chemotherapy or immunotherapy, may enhance therapeutic outcomes while reducing systemic toxicity. Evaluating these combinatorial strategies in advanced and metastatic HCC models could provide insights into the clinical potential of this targeted approach. Additionally, investigating the immunomodulatory effects of localized thermal ablation on the tumor microenvironment may reveal synergistic mechanisms that could improve treatment responses and reduce recurrence rates.

Conclusions

The GNPs-PEI-FA-Cad-1 system represents a promising platform for targeted molecular therapy in hepatocellular carcinoma. The therapy enabled selective ablation of tumor tissue while preserving healthy liver parenchyma**,** confirmed by histological analysis and improved serum biomarkers.

The system showed excellent colloidal stability, appropriate size for tumor accumulation, and successful functionalization, ensuring targeted delivery.

The chemically induced HCC model using DEN combined with CCl_4 proved effective and reproducible in gradually generating liver tumors in *Mus musculus* mice, providing a realistic and well-suited biological framework for testing novel therapies.

Gold nanoparticle-mediated photothermal therapy, activated by near-infrared radiation, showed encouraging levels of specificity and efficacy in this HCC model.

Together, these findings validate both the animal model and the therapeutic potential of the applied nanostructured strategy. The results highlight the synergistic value of combining experimental tumor biology with nanotechnology, offering a solid foundation for the development of innovative therapeutic protocols for HCC and potentially other cancers resistant to conventional treatments.

Acknowledgements

The authors wish to acknowledge financial support from the Iuliu Hatieganu University of Medicine and Pharmacy, Cluj-Napoca, Romania, grant contract no. 1680/54/19.01.2018.

Authors' contributions

M.C. and L.M. contributed to the conception and design of the study. T.M, T.P., and O.M. collected the data. T.M. performed the statistical analysis. R.P., F.T., and M.C. conducted lab analyses and interpreted results, M.C. drafted the manuscript. All authors critically reviewed, approved the final version, and agreed to be accountable for the work.

References

1. International Agency for Research on Cancer. Global Cancer Observatory: Cancer Today. World Health Organization. Available from: https://gco.iarc.fr/today n.d.
2. Hwang SY, Danpanichkul P, Agopian V, Mehta N, Parikh ND, Abou-Alfa GK, et al. Hepatocellular carcinoma: updates on epidemiology, surveillance, diagnosis and treatment. Clin Mol Hepatol. 2025;31:S228-S254.
3. Yuan Y, Sun W, Xie J, Zhang Z, Luo J, Han X, et al. RNA nanotherapeutics for hepatocellular carcinoma treatment. Theranostics. 2025;15:965-992.

4. Ikeda M, Morizane C, Ueno M, Okusaka T, Ishii H, Furuse J. Chemotherapy for hepatocellular carcinoma: current status and future perspectives. Jpn J Clin Oncol. 2018;48:103-114.
5. Saha S, Taneja M, Dubey S, Bhardwaj A. Unlocking the potential of gold nanoparticles as a game-changer in the fight against hepatocellular carcinoma. Explor Med. 2025;6:1001272.
6. Liu YA, Liang BY, Guan Y, You J, Zhu L, Chen XP, et al. Loss of N-cadherin is associated with loss of E-cadherin expression and poor outcomes of liver resection in hepatocellular carcinoma. J Surg Res. 2015;194:167-176.
7. Rodriguez FJ, Lewis-Tuffin LJ, Anastasiadis PZ. E-cadherin's dark side: possible role in tumor progression. Biochim Biophys Acta. 2012;1826:23-31.
8. Hu QP, Kuang JY, Yang QK, Bian XW, Yu SC. Beyond a tumor suppressor: Soluble E-cadherin promotes the progression of cancer. Int J Cancer. 2016;138:2804-2312.
9. Xiao K, Allison DF, Kottke MD, Summers S, Sorescu GP, Faundez V, et al. Mechanisms of VE-cadherin processing and degradation in microvascular endothelial cells. J Biol Chem. 2003;278:19199-19208.
10. Quevedo-Ocampo J, Escobedo-Calvario A, Souza-Arroyo V, Miranda-Labra RU, Bucio-Ortiz L, Gutiérrez-Ruiz MC, et al. Folate Metabolism in Hepatocellular Carcinoma. What Do We Know So Far? Technol Cancer Res Treat. 2022;21:15330338221144446.
11. Szwed M, Jost T, Majka E, Gharibkandi NA, Majkowska-Pilip A, Frey B, et al. Pt-Au Nanoparticles in Combination with Near-Infrared-Based Hyperthermia Increase the Temperature and Impact on the Viability and Immune Phenotype of Human Hepatocellular Carcinoma Cells. Int J Mol Sci. 2025;26:1574.
12. Badir A, Refki S, Sekkat Z. Utilizing gold nanoparticles in plasmonic photothermal therapy for cancer treatment. Heliyon. 2025;11:e42738.
13. Kimling J, Maier M, Okenve B, Kotaidis V, Ballot H, Plech A. Turkevich method for gold nanoparticle synthesis revisited. J Phys Chem B. 2006;110:15700-15707.
14. Arifin WN, Zahiruddin WM. Sample Size Calculation in Animal Studies Using Resource Equation Approach. Malays J Med Sci. 2017;24:101-105.
15. Amorim I, Taulescu MA, Ferreira A, Rêma A, Reis CA, Faustino AM, et al. An immunohistochemical study of canine spontaneous gastric polyps. Diagn Pathol. 2014;9:166.
16. Meuten DJ. Tumors in domestic animals. John Wiley & Sons; 2020:202-322.
17. Heindryckx F, Colle I, Van Vlierberghe H. Experimental mouse models for hepatocellular carcinoma research. Int J Exp Pathol. 2009;90:367-386.
18. Chung SI, Moon H, Ju HL, Cho KJ, Kim DY, Han KH, et al. Hepatic expression of Sonic Hedgehog induces liver fibrosis and promotes hepatocarcinogenesis in a transgenic mouse model. J Hepatol. 2016;64:618-627.
19. Vesselinovitch SD, Mihailovich N. Kinetics of diethylnitrosamine hepatocarcinogenesis in the infant mouse. Cancer Res. 1983;43:4253-4259.
20. Rao KV. Distribution pattern of the major exploited marine fishery resources of India. In: Proceedings of the symposium on living resources of the seas around India, Mandapam Camp. 1973.
21. Kumar et al., Robbins & Cotran Pathologic Basis of Disease, 10th ed. Elsevier, 2020
22. Zhou F, Yang S, Zhao C, Liu W, Yao X, Yu H, et al. γ-Glutamyl transpeptidase-activatable near-infrared nanoassembly for tumor fluorescence imaging-guided photothermal therapy. Theranostics. 2021;11:7045-7056.
23. Li H, Yao Q, Xu F, Xu N, Sun W, Long S, et al. Lighting-Up Tumor for Assisting Resection via Spraying NIR Fluorescent Probe of γ-Glutamyltranspeptidas. Front Chem. 2018;6:485.
24. Ebaid H, Bashandy SA, Alhazza IM, Rady A, El-Shehry S. Folic acid and melatonin ameliorate carbon tetrachloride-induced hepatic injury, oxidative stress and inflammation in rats. Nutr Metab (Lond). 2013;10:20.
25. Antelava NA, Gogoluari MI, Gogoluari LI, Pirtskhalaĭshvili NN, Okudzhava MV. [Efficacy and safety of heptral, vitamin B6 and folic acid during toxic hepatitis induced by CCL4]. Georgian Med News. 2007:53-56.